Electronic Supplementary Material (ESI) for ChemComm.

Supporting information

Unravelling the water adsorption in a robust iron carboxylate metal organic framework

Dirk Lenzen, [a] Jakob G. Eggebrecht, [b] Paulo G.M. Mileo, [c] Dominik Fröhlich, [d] Stefan Henninger, [d] Cesare Atzori, [e] Francesca Bonino, [e] Alexandra Lieb, *[b] Guillaume Maurin *[c] and Norbert Stock *[a]

List of Content

1. Experimental

1.1. Materials and methods

All chemicals ($FeCl_3 \cdot 6H_2O$, NaOH, isophthalic acid *m*-H_2BDC) were used as received. A PXRD pattern of a capillary filled with Fe-MIL-59 and activated at 80 °C and 10^{-2} mbar for 1 h was collected on a Stoe Stadi P diffractometer in transmission geometry equipped with Cu-$K_{\alpha 1}$ radiation. PXRD measurements at different relative humidity values were carried out on a PANalytical Empyrean powder diffractometer, using Cu-$K_{\alpha 1+2}$ radiation and a PIXcel detector. The diffractometer was equipped with an Anton Paar CHC^+ humidity chamber with reflection geometry to generate a nitrogen stream with selected, constant relative humidity values at 25 °C. Twelve measurements were carried out at different relative humidity values (ten during adsorption, two during desorption). Structure refinements using the Rietveld method were performed with the program TOPAS Academic v6.0. Variable temperature powder X-ray diffraction (VT-PXRD) patterns were recorded in open capillaries on a Stoe Stadi P Combi diffractometer in transmission geometry equipped with a capillary furnace (Mo-$K\alpha_1$ radiation). Nitrogen and H_2O sorption isotherms were measured at -196 °C and 25 °C, respectively, with a BELSORP-Max apparatus. MeOH and CO_2 sorption isotherms were obtained with a Quantachrome Autosorb at 25, 40 and 60 °C (MeOH) and a VStar at 0 °C (CO_2). Water cycling stabilities were examined in a Setaram^{TM} TGA-DSC-111 on powdered samples. A humidified argon gas flow (40 °C, 76.3 % relative humidity) was generated by a Setaram WetSys humidity controller and passed through the sample chamber, while the temperature of the sample was varied and the mass of the adsorbent was monitored. For the multi-cycle ad-/desorption experiments, the temperature of the sample was varied between 40 °C and 140 °C with a cycle time of 200 min.

Thermogravimetric measurements between room temperature and 600 °C were carried out on a Netzsch STA-409CD (heating rate = 4 K min^{-1}, air flow = 20 mL min^{-1}). Elemental analysis were measured on a HEKAtech Euro EA Elemental Analyzer (CHNS). Energy-dispersive X-ray (EDX) spectroscopy data were recorded on a Philips XL30 FEG microscope. Each sample was measured three times at different spots. From the data the average values in at% of Fe, Cl were calculated (Tab. S1.1).

1.2. Synthetic procedure

The title compound $[Fe_3(\mu_3\text{-}O)(C_8O_4H_4)_3(OH,Cl)(H_2O)_2] \cdot xH_2O$, x = 0-10) has been synthesized in water under reflux.

250 ml scale synthesis. The synthesis at 12 g scale was carried out in a 500 mL round bottom flask. Initially, aqueous solutions of *m*-Na_2BDC (100 mL, 0.5 mol/L, 50 mmol) and $FeCl_3$ (100 mL, 0.5 mol/L, 50 mmol) were mixed under stirring with 50 mL deionised water forming an orange X-ray amorphous precipitate. This slurry was heated for 6 h under reflux conditions. After hot filtration, multiple washing steps were carried out, stirring the sample in 250 mL hot water for 1 h each time. This leads to the removal of Cl^- ions in the sample (Tab. S1.1). Filtering and subsequent drying at 100 °C results in 11.51 g of an orange product, which corresponds to a yield of 95 wt% (based on the chemical formula $[Fe_3(\mu_3\text{-}O)(C_8O_4H_4)_3(OH)(H_2O)_2]$).

5 L scale synthesis. The synthesis at 250 g scale was carried out in a 10 L round bottom flask as described in the previous section. Aqueous solutions of *m*-Na_2BDC (2

L, 0.5 mol/L, 1 mol) and $FeCl_3$ (2 L, 0.5 mol/L, 1 mol) were mixed with 1 L of deionised water.

Elemental analysis for the composition $[Fe_3O\ (C_8O_4H_4)_3(OH)(H_2O)_2]\cdot 9H_2O)$: $C_{obs/calc}$ (32.2/32.4), $H_{obs/calc}$ (3.6/4.0).

Tab. S1.1 – Results of the EDX analyses of three differently synthesized Fe-MIL-59 samples after multiple washing steps (-Wx, x = 1 to 5) consisting of stirring the sample in hot water for 1 h each time. Thorough washing leads to an almost quantitative removal of Cl^- ions.

Sample	Cl [at%]	Fe [at%]	chloride to hydroxide ratio		
Fe-MIL-59-1-as	20.37	79.65	0.77	:	0.23
Fe-MIL-59-1-W1	18.30	81.70	0.67	:	0.33
Fe-MIL-59-1-W2	16.90	83.10	0.61	:	0.39
Fe-MIL-59-1-W3	15.75	84.20	0.56	:	0.44
Fe-MIL-59-1T-W4	8.20	91.80	0.27	:	0.73
Fe-MIL-59-1-W5	1.58	98.54	0.05	:	0.95
Fe-MIL-59-2-as	23.08	76.92	0.90	:	0.10
Fe-MIL-59-2-W1	20.82	79.18	0.79	:	0.21
Fe-MIL-59-2-W2	15.40	84.57	0.55	:	0.45
Fe-MIL-59-3-as	22.62	77.36	0.88	:	0.12
Fe-MIL-59-3-W1	20.55	79.45	0.78	:	0.22
Fe-MIL-59-3-W2	16.96	83.04	0.61	:	0.39

2. Structure refinements of Fe-MIL-59 treated at different relative humidity values

As a starting point for the refinement the structure of V-MIL-59 was used.[1] The refinements were carried out using the program Topas Academics 4 employing only restraints but no constrains. The PXRD measurements were carried out on a PANalytical empyrean powder diffractometer, using Cu-$K_{\alpha1+2}$ radiation and a PIXcel detector. The diffractometer was equipped with an Anton Paar CHC^+ humidity chamber with reflection geometry to generate a nitrogen stream with selected, constant relative humidity values at 25 °C. Twelve measurements were carried out at different relative humidity values (ten during adsorption, two during desorption). Additionally a capillary filled with Fe-MIL-59 was activated at 80 °C and 10^{-2} mbar for 1 h and powder diffraction data was collected on a Stoe Stadi P diffractometer in transmission geometry equipped with Cu-$K_{\alpha1}$ radiation, a curved germanium monochromator and a linear MYTHEN detector with an aperture angle of 17°. The crystallographic data is given in Tab. S2.1.

Tab. S2.1 – Crystallographic details of the Fe-MIL-59 structures determined at different relative humidity values (p/p_0).

p/p_0	Space group	*a* [Å]	*V* [Å³]	r_{wp}	GOF
capillary ⇒ approx. 0	$Pa\bar{3}$	19.0027(8)	6862.0(8)	2.56	1.70
0.007	$Pa\bar{3}$	19.1467(3)	7019.0(3)	2.08	1.51
0.05	$Pa\bar{3}$	19.1701(3)	7044.9(3)	1.94	2.24
0.10	$Pa\bar{3}$	19.2055(2)	7084.0(3)	1.92	2.23
0.13	$Pa\bar{3}$	19.2199(2)	7100.0(3)	1.92	2.21
0.15	$Pa\bar{3}$	19.2137(2)	7093.0(2)	2.18	2.43
0.21	$Pa\bar{3}$	19.2127(2)	7091.9(2)	2.20	2.43
0.30	$Pa\bar{3}$	19.2155(2)	7095.0(2)	2.35	1.92
0.37	$Pa\bar{3}$	19.2174(2)	7097.2(2)	2.30	1.88
0.42	$Pa\bar{3}$	19.2189(2)	7098.8(2)	2.34	1.90
0.60	$Pa\bar{3}$	19.2228(2)	7103.2(2)	2.30	1.89
0.20*	$Pa\bar{3}$	19.2127(2)	7092.0(2)	2.29	1.87
0.10*	$Pa\bar{3}$	19.2015(3)	7079.5(3)	2.27	1.90

* desorption cycle

For different relative humidity values, different occupancies of the oxygen atoms inside the pores of the structure were obtained. There are four occupied water positions in the fully loaded Fe-MIL-59 structure named OW1 to OW4. OW1 and OW2 are located in the large pore and OW3 and OW4 in the small pore. From $p/p_0 \geq 0.13$ an additional electron density peak (denoted A5) is observed at the special position ½ ½ 0, often observed during the refinement in highly symmetric cubic space groups. This electron density was not taken into account in the structure discussion, as it does not represent a reasonable atomic position. OW1 is connected to two terminal oxygen atoms of the trinuclear FeO cluster (O5) via hydrogen bonds. OW2 forms hydrogen bonds to OW1 and to O5. OW3 and OW4 are not connected to the framework of the MOF structure but form hydrogen bonds mainly among each other. OW3 water molecules are connected via hydrogen bonds to three different OW4 water molecules, which form OW4 triangles around OW3. OW4 also forms hydrogen bonds to OW1 and connects the water clusters of the two different pore types through their common window. The occupancies of OW1 to 4 are given in Tab. S2.2.

Tab. S2.2 – Crystallographic details of the water guest molecules in the Fe-MIL-59 · 10 H_2O structure determined at different realtive humiditiy values (p/p_0). A bar (-) corresponds to no electron density peak in the Fourier map.

p/p_0	**water/chemical formula**	**water uptake**	**occupancy factor**			
	[OW1-4]	[$g_{H2O}/g_{sorbent}$]	**OW1**	**OW2**	**OW3**	**OW4**
H_2O / formula unit			3	3	1	3
capillary ⇒ approx. 0	1.2	0.03	-	0.39(4)	-	-
0.007	3.6	0.09	0.79(2)	0.43(2)	-	-
0.05	4.3	0.11	0.87(2)	0.56(2)	-	-
0.10	5.2	0.13	0.98(2)	0.74(2)	-	-
0.13	5.3	0.13	1	0.76(2)	-	-
0.15	9.5	0.24	1	1	1	0.86(2)
0.21	10.0	0.25	1	1	1	0.99(1)
0.30	10.0	0.25	1	1	1	1
0.37	10.0	0.25	1	1	1	1
0.42	10.0	0.25	1	1	1	1
0.60	10.0	0.25	1	1	1	1
0.20*	10.0	0.25	1	1	1	1
0.10*	6.0	0.15	0.96(2)	0.86(2)	-	-

* desorption cycle

The oxygen-oxygen distances inside the pores of the Fe-MIL-59 structures are given in Tab. S2.3. The atoms OW1 and OW2 have direct hydrogen bonding contacts to the framework of Fe-MIL-59, OW3 and OW4 are only connected to other water molecules.

Tab. S2.3 – Atomic distances between the oxygen atoms of the water molecules on different crystallographic sites inside the pores to each other and to framework oxygen atoms of Fe-MIL-59.

p/p_0	O5-OW1 [Å]	O5-OW2 [Å]	OW1-OW2 [Å]	OW2-OW2 [Å]	OW3-OW4 [Å]	OW1-OW4 [Å]
capillary ⇒ approx. 0	-	2.5(2)	-	2.8(2)	-	-
0.007	2.40(2) 2.89(2)	2.59(2)	2.65(2) 2.56(2)	2.58(2)	-	-
0.05	2.58(2) 2.87(2)	2.56(2)	2.57(2) 2.70(2)	2.55(2)	-	-
0.10	2.76(2) 2.84(2)	2.64(2)	2.57(2)	2.59(2)	-	-
0.13	2.60(2) 2.89(2)	2.87(2)	2.57(2)	2.70(2)	-	-
0.15	2.72(2) 2.82(2)	2.95(2)	2.55(2)	-	2.82(2)	3.03(3)
0.21	2.75(2) 2.80(2)	2.91(2)	2.58(2)	-	2.75(2)	3.06(2)
0.30	2.76(2) 2.86(2)	2.89(2)	2.59(2)	-	2.75(2)	3.06(2)
0.37	2.77(2) 2.78(2)	2.88(2)	2.67(2)	-	2.76(2)	3.07(2)
0.42	2.74(2) 2.80(2)	2.93(2)	2.65(2)	-	2.93(2)	3.06(3)
0.60	2.69(2) 2.84(2)	2.88(2)	2.61(2)	-	2.70(2)	3.12(2)
0.20*	2.70(2) 2.81(2)	2.91(2)	2.60(3)	-	2.76(2)	3.06(3)
0.10*	2.69(3) 2.72(3)	2.89(3)	2.49(3)	2.56(3)	-	-

* desorption cycle

For the structure determined at the highest relative humidity ($p/p_0 = 0.6$) the atomic distances are given in Tab. S2.4. The figures given in the main manuscript and the Fig. S2.1 are based on this refinement.

Tab. S2.4 – Atomic distances within the framework of Fe-MIL-59 ($p/p_0 = 0.6$).

Atom 1	Atom 2	Distance [Å]	Atom 1	Atom 2	Distance [Å]
Fe1	O1	1.903	C1	C3	1.581
	O2	1.938	C2	C7	1.560
	O3	1.940	C3	C8	1.385
	O4	1.989		C4	1.390
	O5	2.029	C4	C5	1.382
	O6	1.910	C5	C6	1.382
O1	C1	1.268	C6	C7	1.389
O2	C1	1.284	C7	C8	1.387
O3	C2	1.255			
O4	C2	1.273			

2.1. Structural details and pore arrangement in Fe-MIL-59

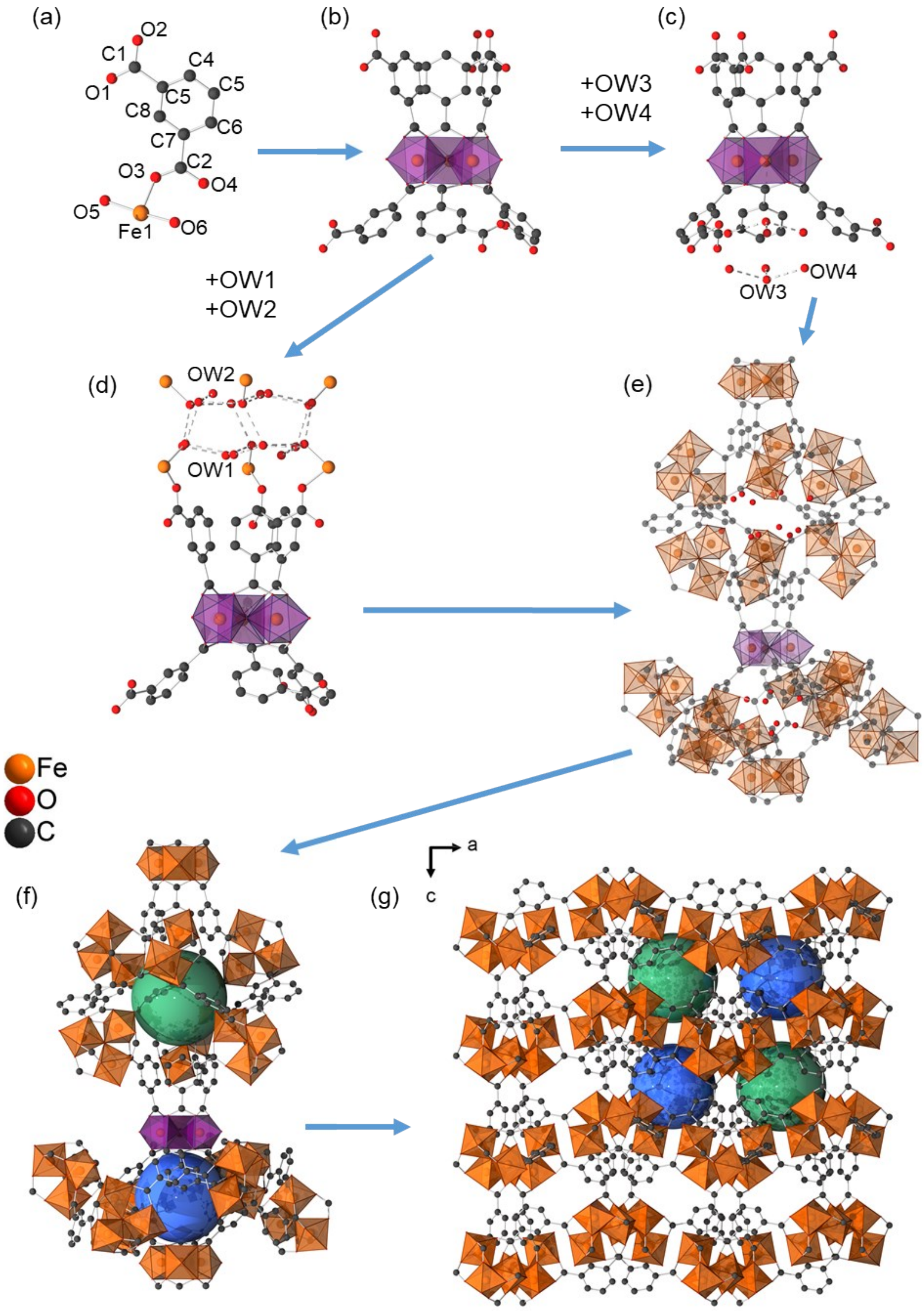

Fig. S2.1 – Water loaded structure ($p/p_0 = 0.6$) of Fe-MIL-59. (**a**) Asymmetric unit. (**b**) Inorganic building unit surrounded by six linker molecules. (**c**) Water molecules in the small pore. Water molecules in the large pore (**d**). (**e**) Section of the structure, with both pore types and using colored spheres (**f**; blue = small pore; green = large pore). (**g**) Larger part of the structure projected along [010].

3. Thermogravimetry

The thermogravimetric measurement was carried out on a Netzsch STA-409CD (heating rate = 4 K min^{-1}, gas flow = 20 mL min^{-1}). The chemical formula Fe-MIL-59 · 10 H_2O leads to a good agreement - within the error range of this measurement method - between the measured and calculated values for the mass losses and residual mass.

A PXRD measurement of the thermal decomposition product was carried out on a Stoe Stadi P diffractometer in transmission geometry equipped with Cu-$K_{\alpha 1}$ radiation, a curved germanium monochromator and a linear MYTHEN detector with an aperture angle of 17°.

Tab. S3.1 – Calculated and measured mass steps for the thermal decomposition of Fe-MIL-59, $[Fe_3(\mu_3\text{-}O)(C_8O_4H_4)_3(OH)(H_2O)_2]$.

Fe-MIL-59 · 10 H_2O	measured [wt. %]	Calculated [wt. %]
step 1: 5 water molecules	9.4	9.9
step 2: 5 water molecules	9.4	9.9
step 3: oxidation of organic linker	52.8	53.8
residual mass [wt%], (Fe_2O_3, #ICSD = 15840)	28.4	26.4

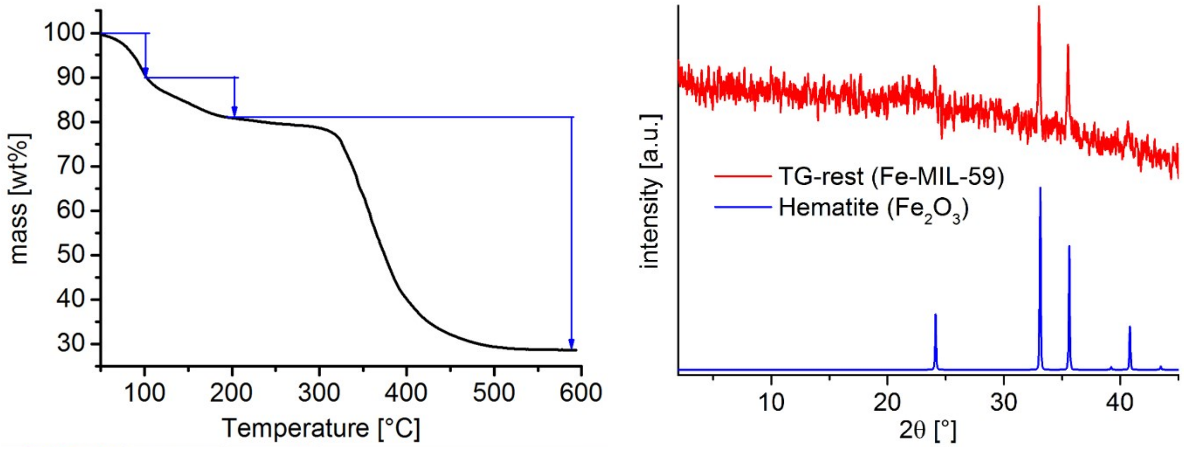

Fig. S3.1 – TG curve of Fe-MIL-59 (left) and PXRD of the residue of the TG measurement and a calculated pattern of Hematite (Fe_2O_3, #ICSD = 15840) for comparison (right).

4. Variable-temperature powder X-ray diffraction (VT-PXRD)

PXRD patterns were recorded in an open capillary on a Stoe Stadi P Combi diffractometer in transmission geometry equipped with Mo-Kα_1 radiation, a curved germanium monochromator and a linear MYTHEN detector with an aperture angle of 17° and a capillary furnace. The measurements were performed between room temperature and 500 °C.

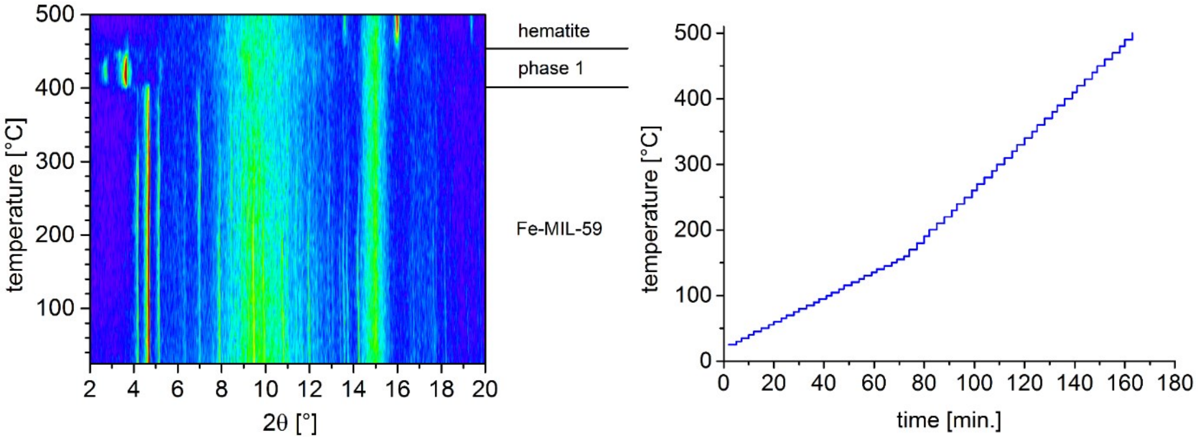

Fig. S4.1 – Results of the VT-PXRD investigation of Fe-MIL-59 (left) and the used temperature program (right).

5. Infrared spectroscopy

IR spectra were recorded to study the de- and adsorption of water in Fe-MIL-59 after thermal treatment of the sample. Fig. S5.1 shows the IR spectrum between 4000 and 400 cm^{-1} collected on a Bruker ALPHA-FT-IR A220/D-01 using an ATR-unit. The other IR spectra (Fig. S5.2) were collected in transmission mode using a Thermo Scientific Nicolet 6700 spectrometer equipped with a liquid N_2 cooled MCT detector on thin self-supporting pellets. The Fe-MIL-59 sample was activated in dynamic high vacuum (10^{-4} mbar) at temperatures of 100 °C over night (~ 16 h) in a homemade quartz cell that allows also controlled dosages of gaseous probe molecules. After activation, small doses of H_2O were added until saturation pressure at room temperature (25 mbar) was reached. After each dosing step, an IR spectrum was recorded. The stability of the samples under the applied conditions (activation and successive water doses) is confirmed by PXRD measurement of the samples.

Prolonged activation of Fe-MIL-59 leads to the desorption of guest species, presumably small amounts of residual linker molecules (isophthalic acid) as indicated by bands between 2500 and 3250 cm^{-1} and water molecules (3400 to 3700 cm^{-1}) (black curves in Fig. S5.2). The addition of water vapour leads to a quite sharp band at about 3660 cm^{-1} followed by a broader signal at about 3475 cm^{-1}. The first one may be assigned to a Fe-OH species, as previously described in literature,[2] while the other one is due to water molecules interacting through H-bonds. It is impossible to observe water at higher coverages (i.e. at $p/p_0 > 0.2$, after the step in the isotherms) as water absorbs IR radiation too much and the spectrum gets too noisy.

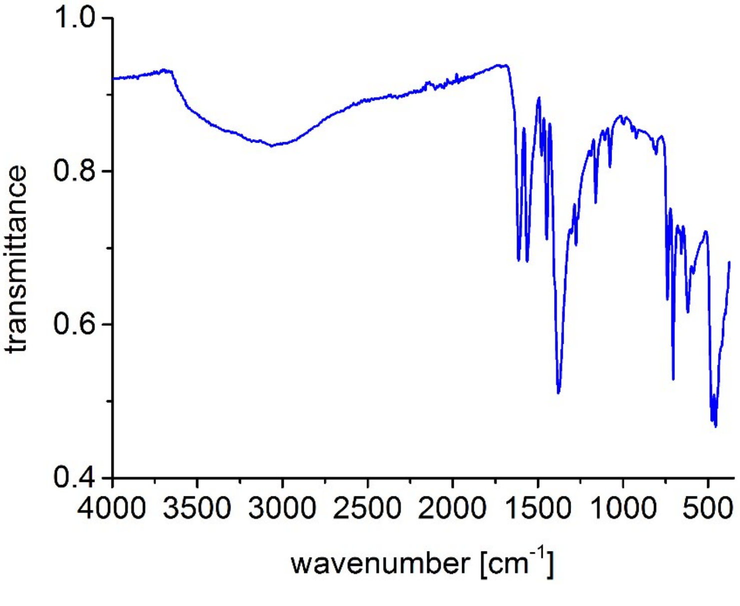

Fig. S5.1 – Infrared spectrum of Fe-MIL-59 recorded at room temperature in air.

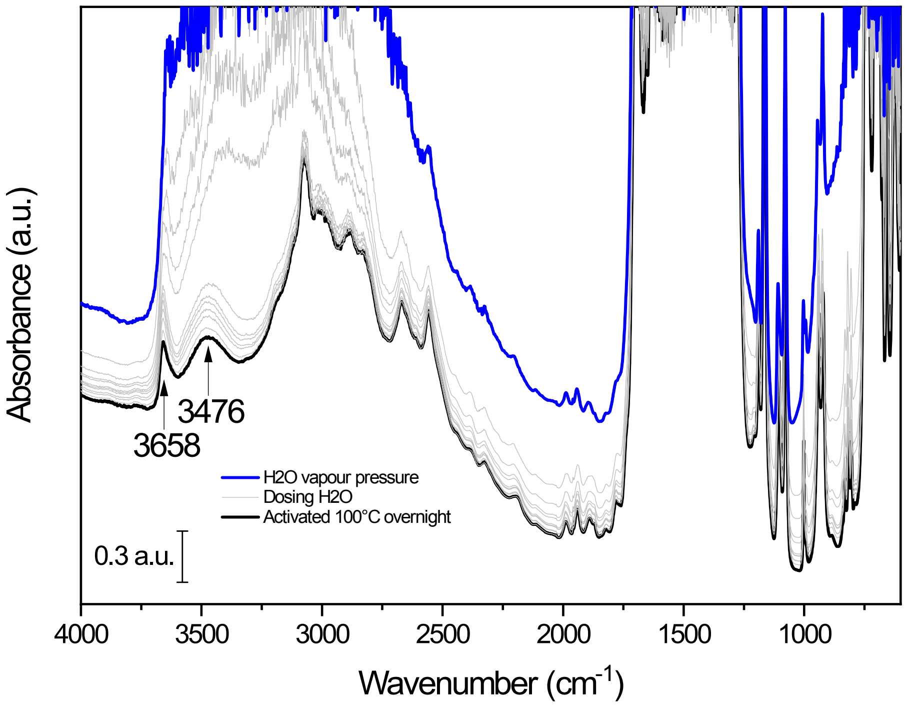

Fig. S5.2 – Infrared spectra of Fe-MIL-59 activated at 100 °C over night (black) and after addition of pulses of water vapor.

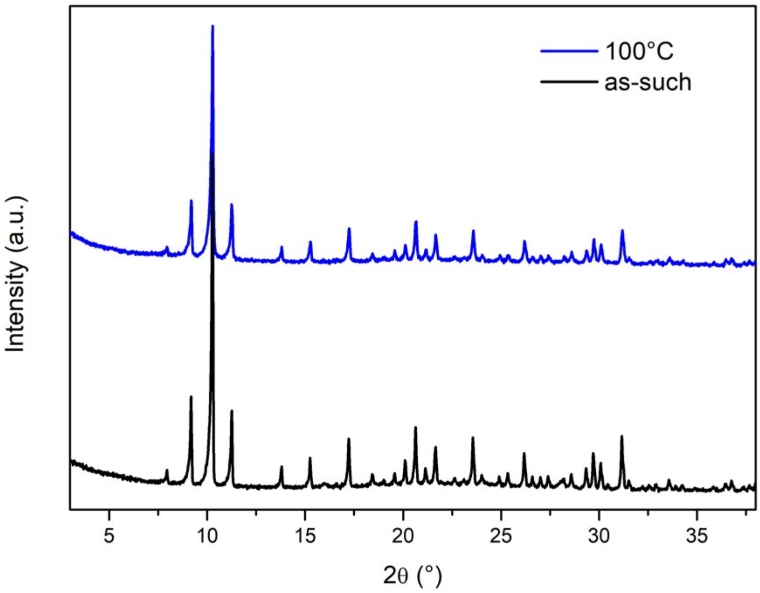

Fig. S5.4 – PXRD patterns of a) the starting material and b) the samples used in the IR experiments treated at 100 °C and successive water doses is confirmed by PXRD measurement of the samples.

6. PXRD Measurements and Rietveld refinement

PXRD patterns used for the structure refinement and localization of the water molecules in the pores of Fe-MIL-59 under different relative pressures (Tab. S2.1) are presented in Fig. S6.1.

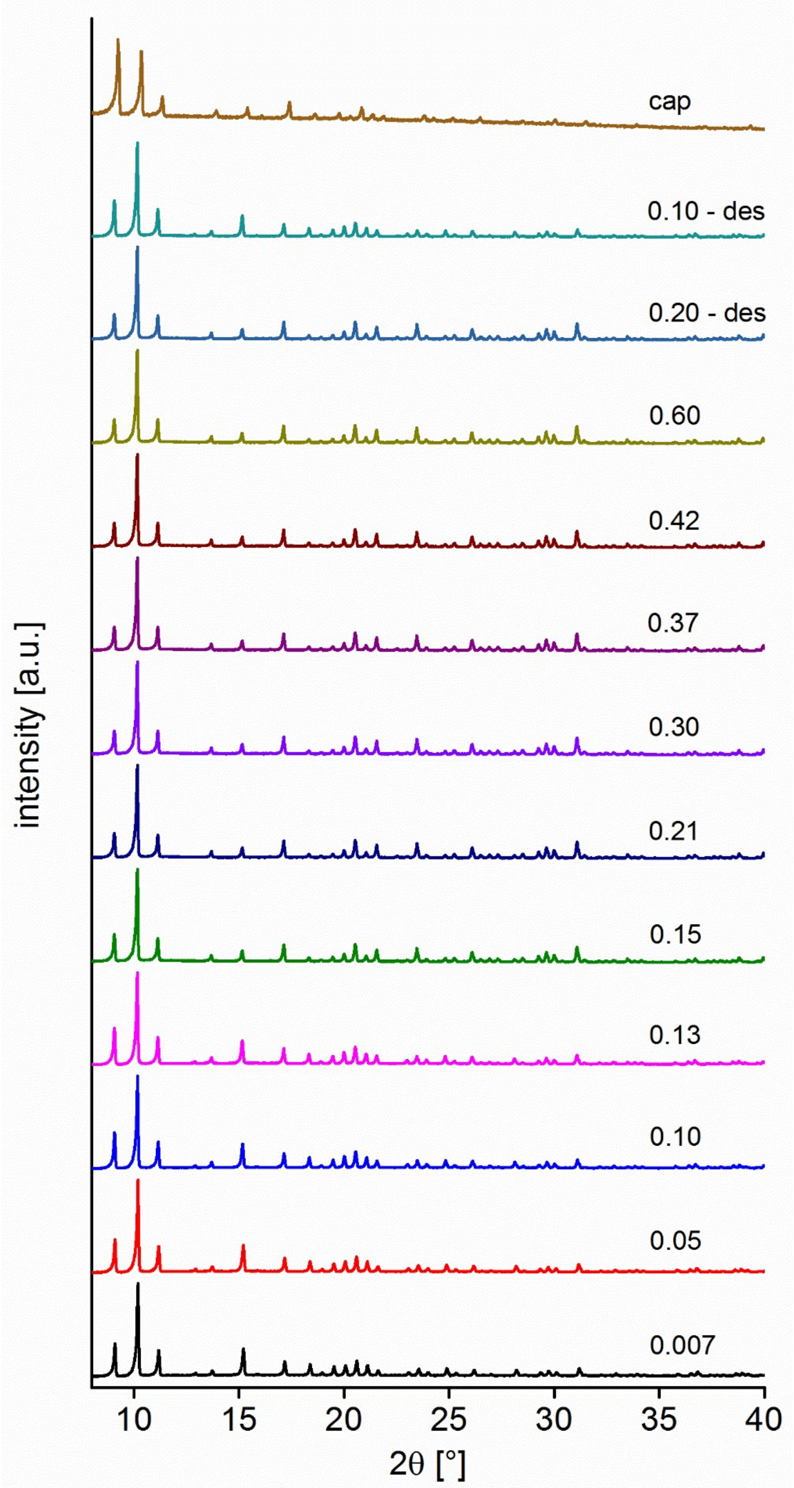

Fig. S6.1a – PXRD patterns of Fe-MIL-59 measured under different relative humidity values. The PXRD pattern labeled cap was collected from a sample in a capillary, which was activated at 80 °C under reduced pressure and subsequently sealed. Changes in relative intensities are due to the different amounts of water molecules in the pores.

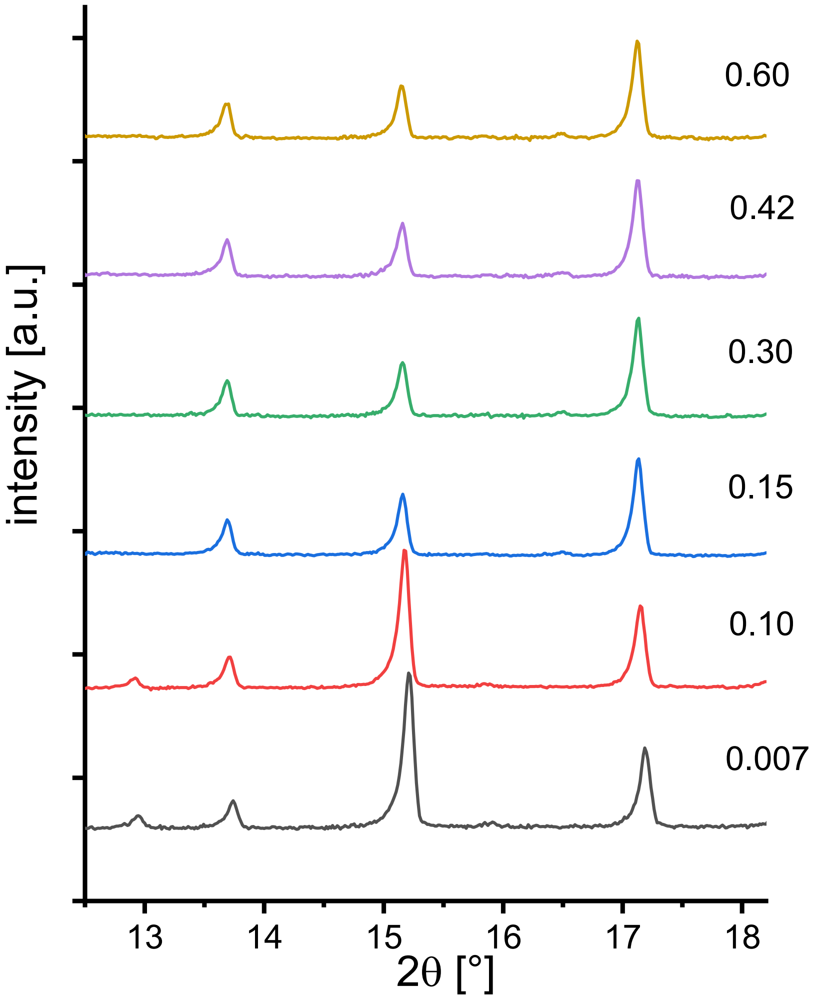

Fig. S6.1b – Section of selected PXRD patterns from Fig. S6.1a from 12.8 to 18.2 ° (2θ). Changes in relative intensities are due to the different amounts of water molecules in the pores.

The Rietveld plots of the refinement of data of Fe-MIL-59 collected at different relative water pressures is given in Fig. S6.2 to S6.14). The CIF data are summarized in a separate document available as supplementary information.

p/p_0 = 0.007, adsorption branch

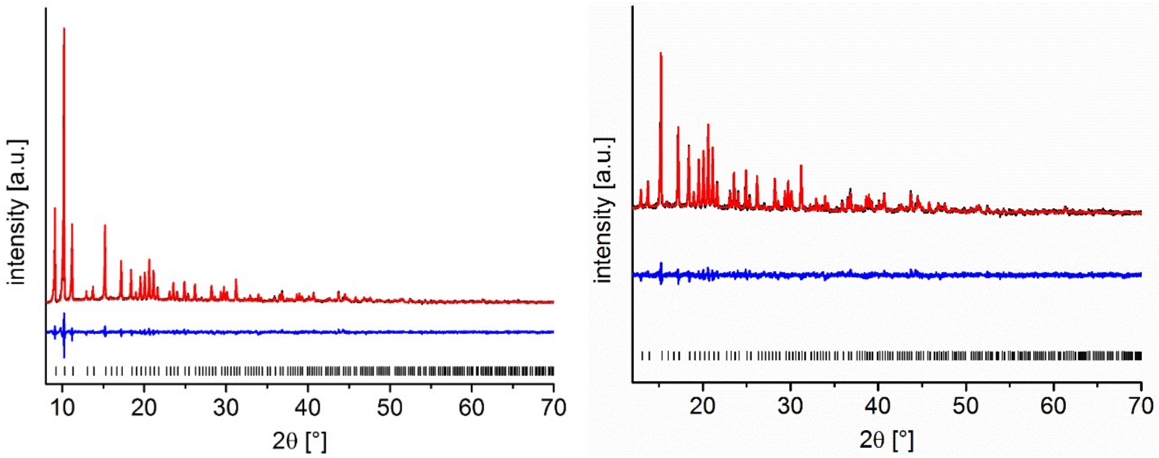

Fig. S6.2 – Rietveld plot of the refinement of data of Fe-MIL-59 collected at a relative water pressure of p/p_0 = 0.007 (black is the measured, red the calculated and blue the difference curve; black lines are the positions of the allowed reflections).

p/p_0 = 0.05, adsorption branch

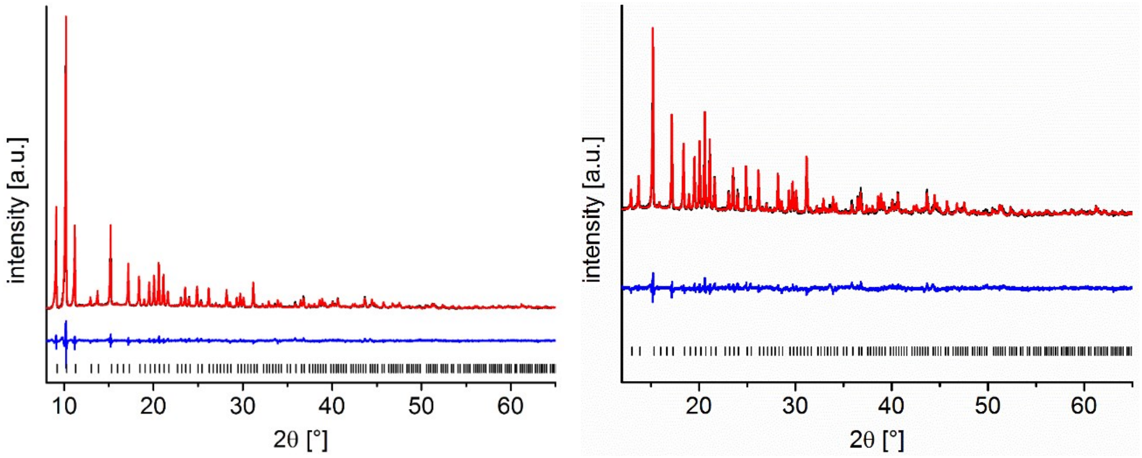

Fig. S6.3 – Rietveld plot of the refinement of data of Fe-MIL-59 collected at a relative water pressure of p/p_0 = 0.05 (black is the measured, red the calculated and blue the difference curve; black lines are the positions of the allowed reflections).

p/p_0 = 0.10, adsorption branch

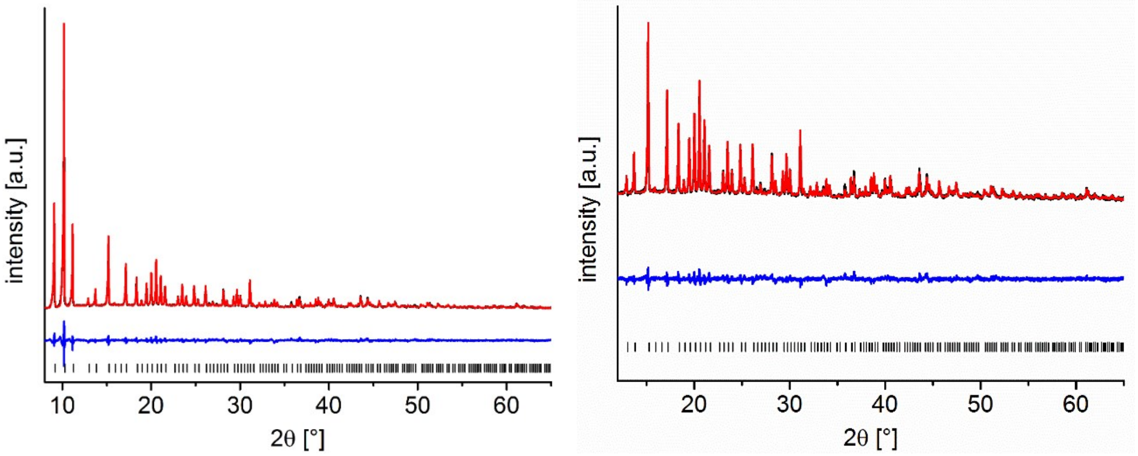

Fig. S6.4 – Rietveld plot of the refinement of data of Fe-MIL-59 collected at a relative water pressure of p/p_0 = 0.10 (black is the measured, red the calculated and blue the difference curve; black lines are the positions of the allowed reflections).

p/p_0 = 0.13, adsorption branch

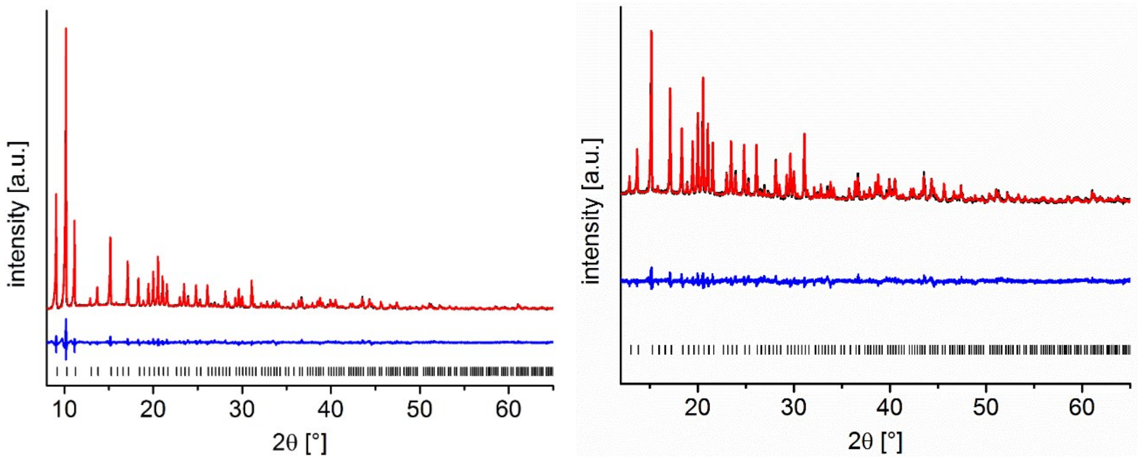

Fig. S6.5 – Rietveld plot of the refinement of data of Fe-MIL-59 collected at a relative water pressure of p/p_0 = 0.13 (black is the measured, red the calculated and blue the difference curve; black lines are the positions of the allowed reflections).

p/p_0 = 0.15, adsorption branch

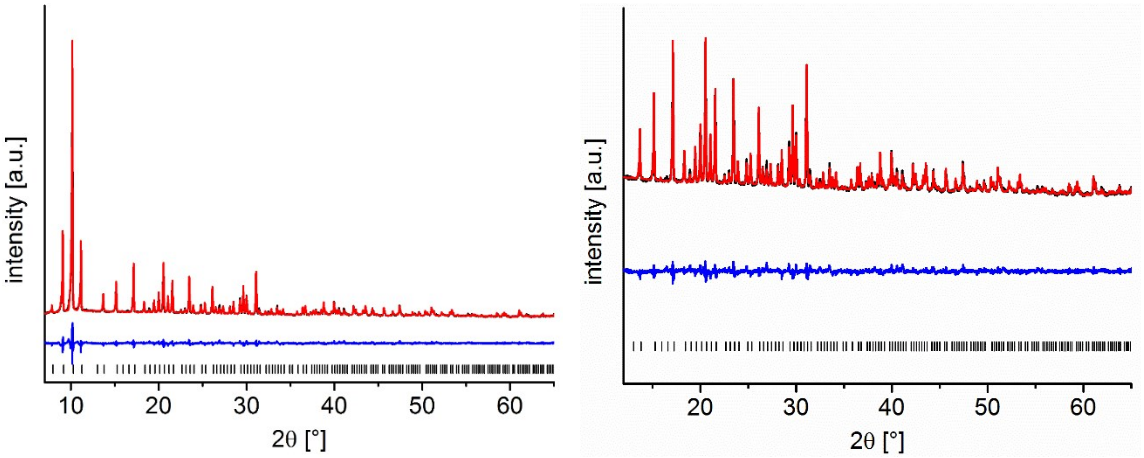

Fig. S6.6 – Rietveld plot of the refinement of data of Fe-MIL-59 collected at a relative water pressure of p/p_0 = 0.15 (black is the measured, red the calculated and blue the difference curve; black lines are the positions of the allowed reflections).

p/p_0 = 0.21, adsorption branch

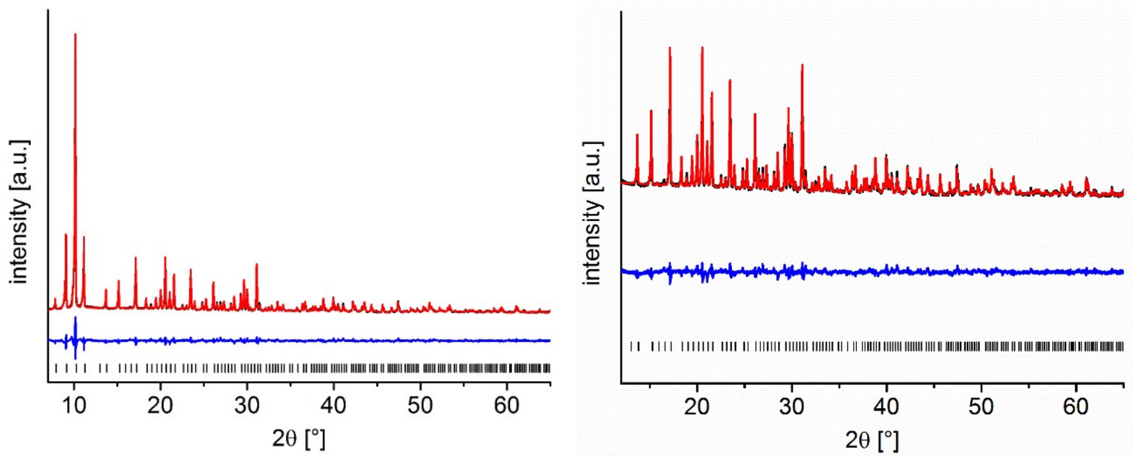

Fig. S6.7 – Rietveld plot of the refinement of data of Fe-MIL-59 collected at a relative water pressure of p/p_0 = 0.21 (black is the measured, red the calculated and blue the difference curve; black lines are the positions of the allowed reflections).

p/p_0 = 0.30, adsorption branch

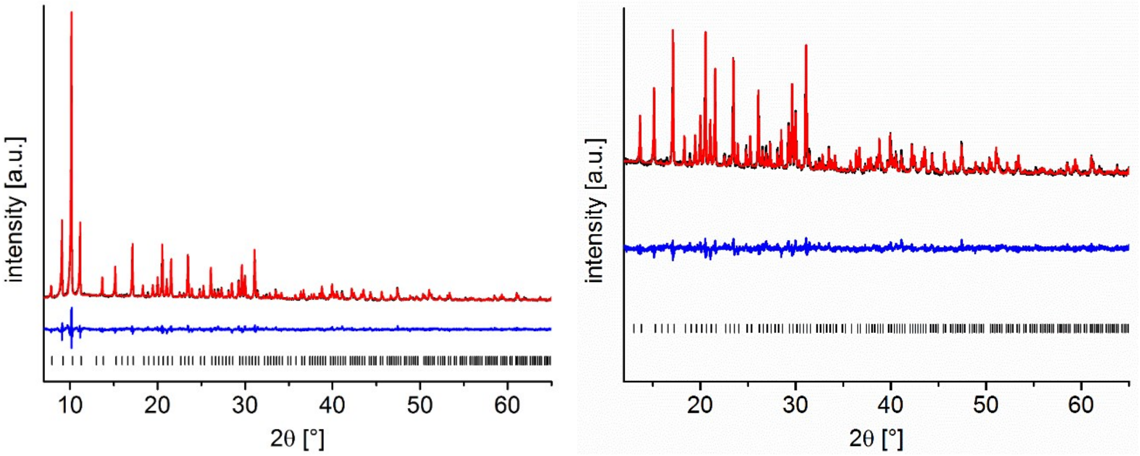

Fig. S6.8 – Rietveld plot of the refinement of data of Fe-MIL-59 collected at a relative water pressure of $p/p_0 = 0.30$ (black is the measured, red the calculated and blue the difference curve; black lines are the positions of the allowed reflections).

p/p_0 = 0.37, adsorption branch

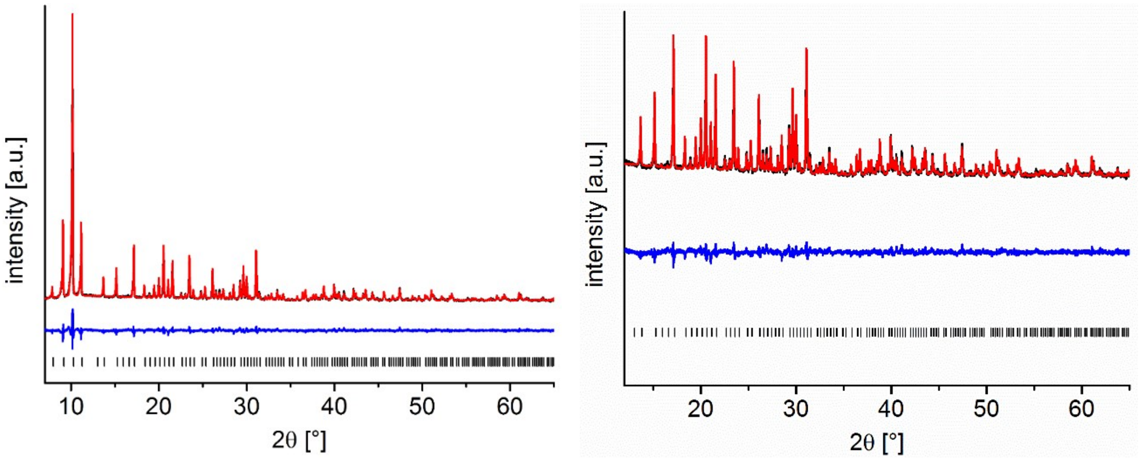

Fig. S6.9 – Rietveld plot of the refinement of data of Fe-MIL-59 collected at a relative water pressure of $p/p_0 = 0.37$ (black is the measured, red the calculated and blue the difference curve; black lines are the positions of the allowed reflections).

$p/p_0 = 0.42$, adsorption branch

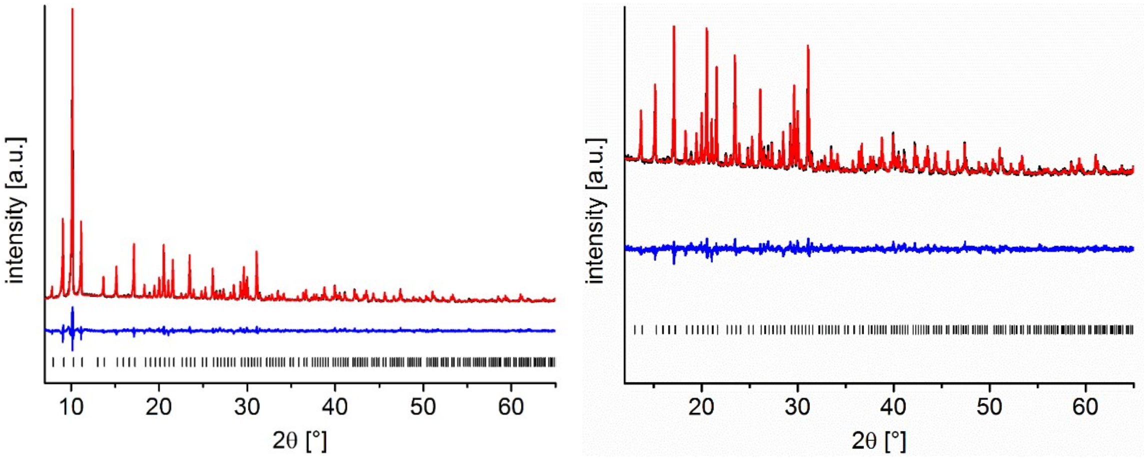

Fig. S6.10 – Rietveld plot of the refinement of data of Fe-MIL-59 collected at a relative water pressure of $p/p_0 = 0.42$ (black is the measured, red the calculated and blue the difference curve; black lines are the positions of the allowed reflections).

$p/p_0 = 0.60$, adsorption branch

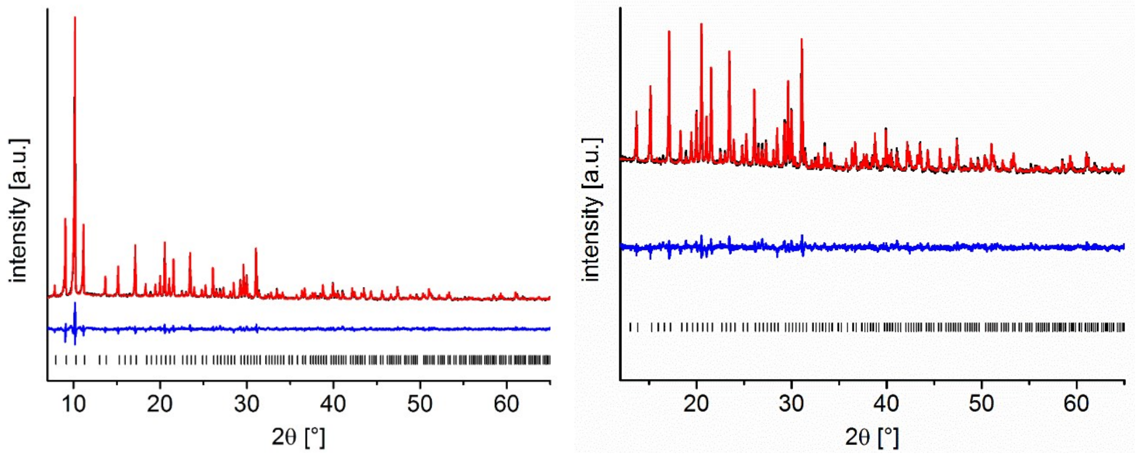

Fig. S6.11 – Rietveld plot of the refinement of data of Fe-MIL-59 collected at relative water pressure of $p/p_0 = 0.60$ (black is the measured, red the calculated and blue the difference curve; black lines are the positions of the allowed reflections).

$p/p_0 = 0.20$, desorption branch

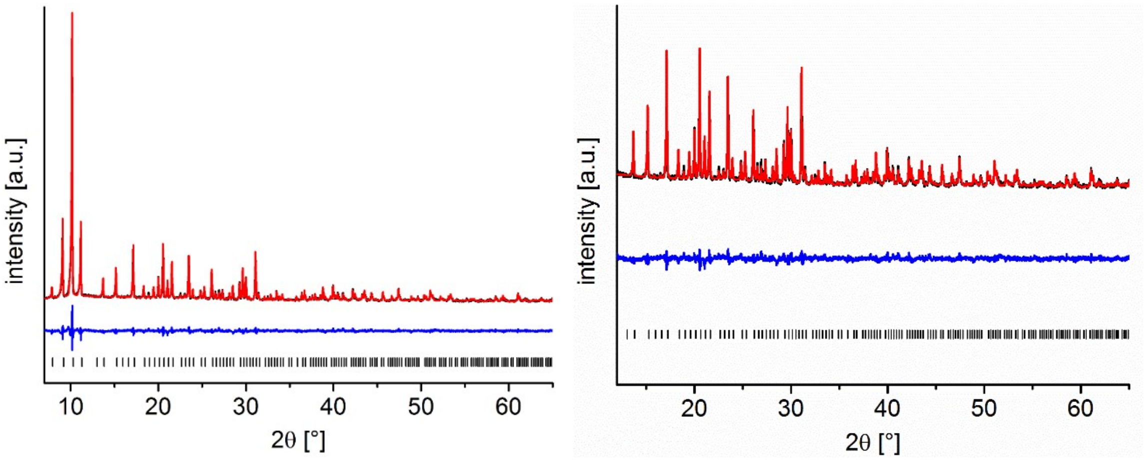

Fig. S6.12 – Rietveld plot of the refinement of data of Fe-MIL-59 collected at a relative water pressure of $p/p_0 = 0.20$ in the desorption curve (black is the measured, red the calculated and blue the difference curve; black lines are the positions of the allowed reflections).

$p/p_0 = 0.10$, desorption branch

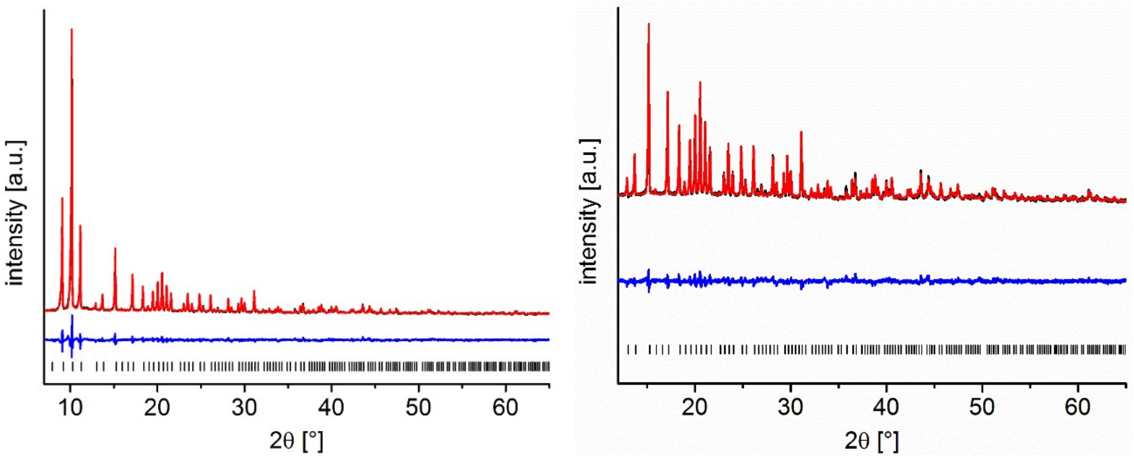

Fig. S6.13 – Rietveld plot of the refinement of data of Fe-MIL-59 collected at a relative water pressure of $p/p_0 = 0.10$ in the desorption curve (black is the measured, red the calculated and blue the difference curve; black lines are the positions of the allowed reflections).

Capillary with Fe-MIL-59, activated for 1 h at 80 °C and 10^{-2} mbar

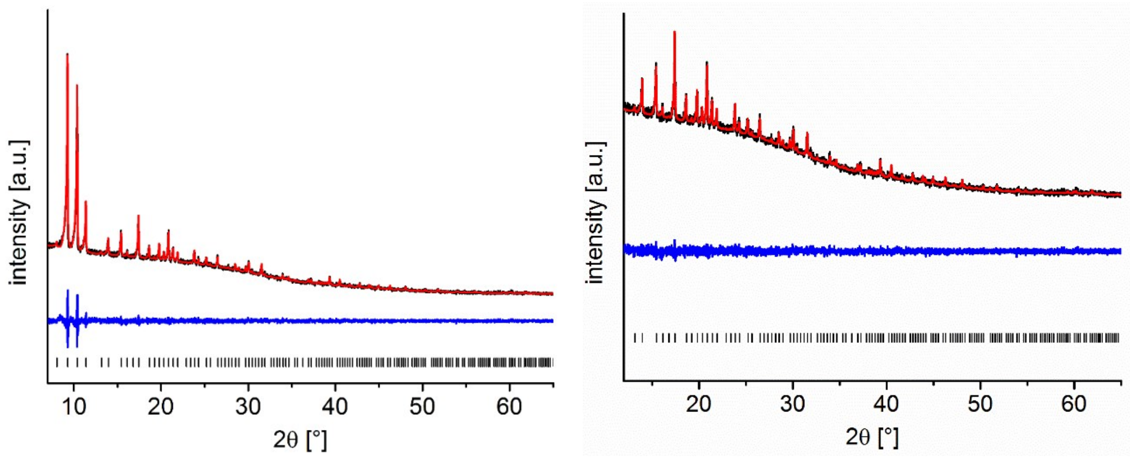

Fig. S6.14 – Rietveld plot of the refinement of data of Fe-MIL-59 collected from a sample in a capillary, which was activated at 80°C at reduced pressure (black is the measured, red the calculated and blue the difference curve; black lines are the positions of the allowed reflections).

7. Sorption measurements

Methanol and carbon dioxide sorption measurements were carried out with a Quantachrome Autosorb at 25, 40 and 60 °C (MeOH) and a VStar at 0 °C (CO_2). Isotherms (Fig. S7.1) were recorded at different temperatures for methanol (25 °C, 40 °C, 60 °C) and carbon dioxide (0 °C) to test a possible application of Fe-MIL-59 for CO_2 capture storage or methanol based adsorption driven chillers.

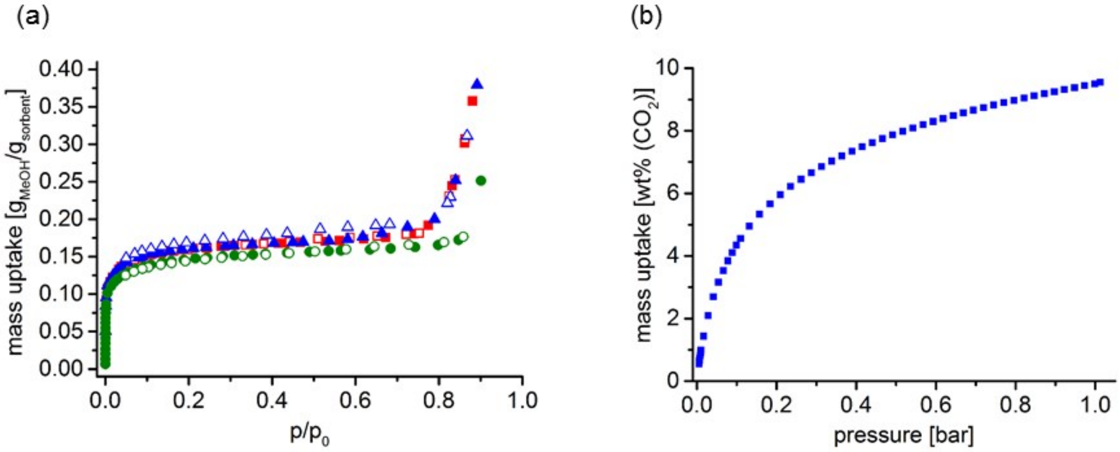

Fig. S7.1 – (a) Methanol sorption isotherms of Fe-MIL-59 at 25 (red squares), 40 (blue triangles) and 60 °C (green dots); (b) carbon dioxide isotherm of at 0 °C. Filled symbols represents adsorption and empty symbols desorption.

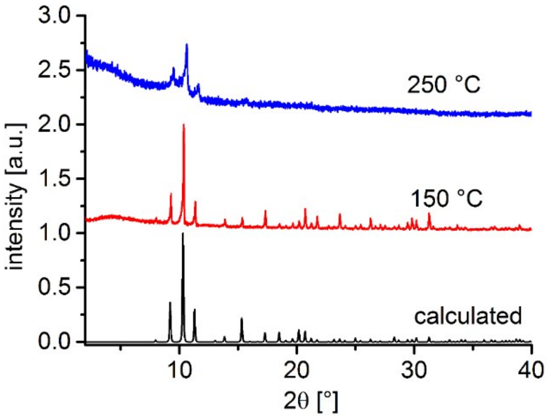

Fig. S7.2 – PXRD patterns of Fe-MIL-59 after a water sorption measurement with an activation temperature of 150 and 250 °C, respectively. A calculated pattern is shown for comparison.

8. Thermogravimetric cycling and stability measurements

Since MIL-59 is stable against H_2O vapor and thermal activation up to 200 °C, its term stability was studied in multi cycle experiments involving 20 adsorption and desorption cycles in an humid atmosphere (relative humidity = 76%). Details have been described previously.[3]

The 20 cycle experiment was carried out in a TG analyzer by thermal cycling (40 - 140 °C) of a sample at a constant relative water pressure of $p/p_0 = 0.76$. This experiment simulates the conditions used in an adsorption driven chiller and gives the total usable uptake (Fig. S8.1). The obtained values show, that ~7 of the 10 adsorbed water molecules can be removed at 140 °C and $p/p_0 = 0.76$. As the pores of Fe-MIL-59 are completely filled again at 40 °C, at $p/p_0 = 0.76$, an amount of 0.18 $g_{H2O}/g_{sorbent}$ can be utilized for a possible ADC application. Equilibrium data of the compound is obtained before and after the cycling measurement by equilibrating the sample during approximately 8 h until no mass change is observed any more. The dry mass is determined by heating the compound to 140 °C in a dried nitrogen stream and the loaded mass at 40 °C at a relative water pressure $p/p_0 = 0.76$. The equilibrium loadings of 0.257 before and 0.247 $g_{H2O}/g_{sorbent}$ after the measurement, respectively, give similar values compared to the isothermal water adsorption measurement. This represents a loss of approx. 4 % within 20 cycles. The loss in uptake capacity could be due to a higher dry mass, whereas the loaded mass remains the same, suggesting no decomposing of the compound during the measurement. The higher dry mass may derive from errors due to the long duration of the measurement routine of more than 100 h, which is known to lead to small signal drifts.

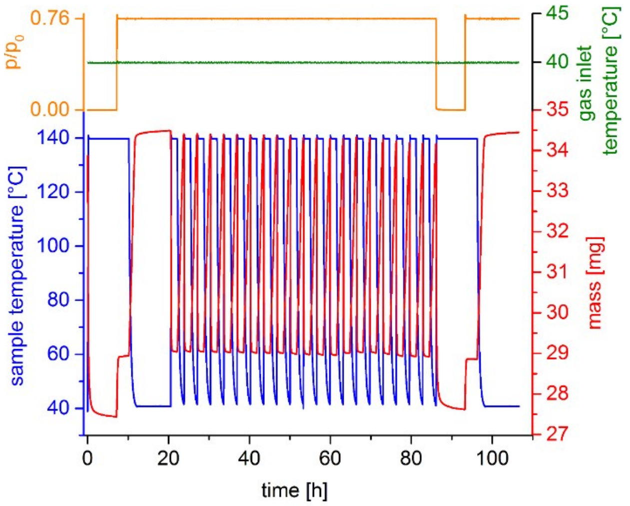

Fig. S8.1 – Results of the cycling TG measurements. Thermal cycling was carried out between 40 and 140 °C at a constant relative water pressure $p/p_0 = 0.76$.

9. Computational studies

The crystal structure of Fe-MIL-59 was initially considered with each Fe-trimer as follows: one Fe atom is bonded to an OH group, while the two others are coordinated to H_2O. This structure was geometry optimized at the Density Functional Theory (DFT) level using the CP2K code keeping the unit cell parameters fixed to the experimental values. The GGA-PBE functional[4] was combined with the triple-ζ valence plus two polarization (TZV2P)[5] basis set for the H, O, and C atoms and with the double-ζ valence plus polarization (DZVP)[6] basis set for the Fe atoms. The van der Waals interactions were also included within the DFT-D3 scheme.[7] Goedecker-Teter-Hutter (GTH) pseudopotentials[8] were employed for all atoms with a plane wave cutoff of 500 Ry and a convergence criterion for the self-consistent field iterations of 10^{-6} Ry. Partial atomic charges were calculated for this structure using the density derived electrostatic and chemical (DDEC) method.[9] This method has demonstrated to give reliable charges for many porous solids, including MOFs.[10]

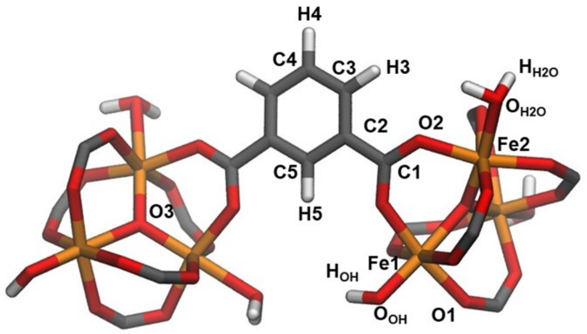

Atom type	q (e)	Atom type	q (e)
O_{OH}	-0.8229	C3	-0.0547
H_{OH}	0.3741	C4	-0.0837
O3	-1.0281	C5	-0.0781
O2	-0..6017	H3	0.1185
O1	-0.5694	H4	0.1046
Fe2	1.4609	H5	0.1249
Fe1	1.4444	O_{H2O}	-0.7272
C1	0.6264	H_{H2O}	0.4168
C2	-0.0592		

Fig. S9.1 – Representation of the different atom types present in the Fe-MIL-59 framework (left) and their respective DFT-calculated partial atomic charges (right). H, C, Fe, and O atoms are represented respectively in white, grey, orange and red.

The interactions between all framework atoms/water molecules and water molecules/water molecules were treated using a van der Waals contribution, modelled by a 12-6 Lennard-Jones (LJ) potential and an electrostatic contribution, represented by a coulombic term. The 12-6 LJ parameters for the atoms of the organic linker were taken from the generic force field DREIDING,[11] while the parameters associated with the inorganic cluster and the oxygen of both the terminal H_2O and of the OH group were taken from the Universal Force Field.[12] Following the treatment adopted in other forcefields,[13]the interactions associated with the polar hydrogens of both terminal water molecules and OH terminal groups were modelled using only electrostatic interactions. The bulk water molecule was described by the TIP4P/2005 model,[14] corresponding to one LJ site centered in the oxygen atom and three charged sites, two centered in the hydrogen atoms and the other in a dummy site 0.1546 Å apart from the oxygen atom. The geometry of the molecule is represented by a O-H bond length of 0.9572 Å and an H-O-H angle of 104.52 Å.

Grand Canonical Monte Carlo (GCMC) simulations were further carried out at 298 K. The simulation box was made of eight conventional unit cells (2×2×2) maintaining the framework atoms fixed in their initial positions. Short-range interactions described by the LJ potential were truncated at a cut-off radius of 12 Å while the Ewald summation approach was used to estimate the Coulombic contribution with a precision of 10^{-6}. For each state point, 2×10^8 Monte Carlo steps following 10^7 equilibration steps have been used. The adsorption enthalpy at low coverage ΔH for water was calculated using the revised Widom's test particle insertion method.[15] In order to gain insight into the configurational distribution of the adsorbed species in the solid, analysis of hydrogen bonds and clusters were also carried out. A hydrogen bond was considered if the distance between the donor (D) and acceptor (A) atoms is shorter than 3.5 Å and the angle formed between the D-A and D-H vectors is lower than 37°. Clusters formed by the water molecules were calculated using a neighboring list algorithm[16] using a critical clustering radius of 3.1 Å.

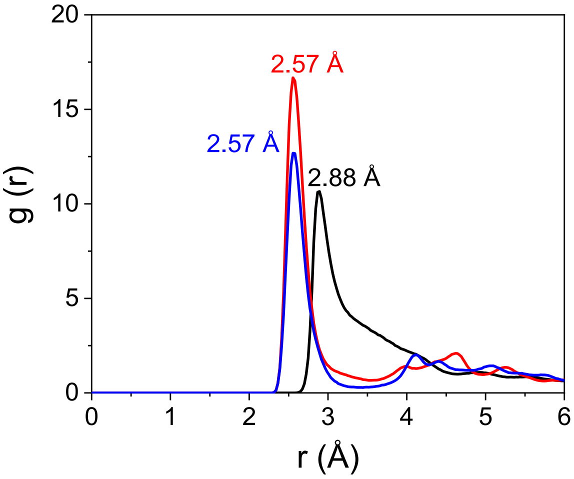

Fig. S9.2 –Radial distribution functions displaying the O - O interacting pairs formed between the adsorbed water molecules and themselves (black line), the terminal OH groups (blue line) and the terminal water molecules (red line) at $p/p_0 = 0.11$.

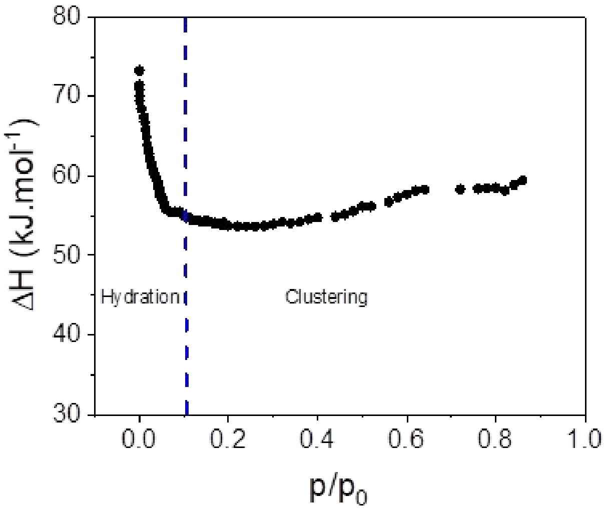

Fig. S9.3 – GCMC simulated adsorption enthalpy for water in Fe-MIL-59 at 298 K.

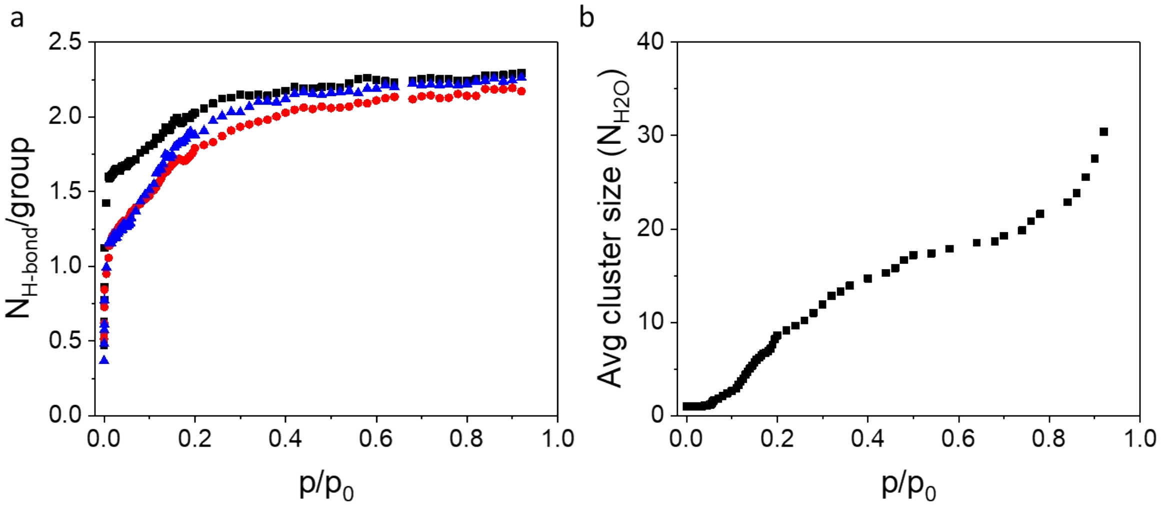

Fig. S9.4 – Evolution of (a) the normalized number of hydrogen bonds per terminal H_2O (black squares), terminal OH groups (red circles), and adsorbed H_2O (blue triangles) and (b) the average cluster size in number of water molecules with the partial pressure.

10. Water adsorption properties of different adsobents

Tab. S10.1 – Summary of material used to study water adsorption properties (n.a. = information not available).

Formula	Capacity	$-\Delta H_{ads}$	p_{rel}[b]	Hysteresis	Stability[c]	Literature
Framework	[g/g]	[kJ/mol]	[p/p_0]			
$[Cr_3O(H_2O)_2F(p\text{-}BDC)_3]$	0.7	46.0	0.4	yes	40 cycles	17,18
$[Cr_3O(H_2O)_2(X^e)(BTC)_2]$	0.5	47.6	0.2-0.5	yes	n.a.	18–20
$[Cr_6O_2Cl_2(H_2O)_4(TCPT)_3]$	1.95	n.a.	0.6	0.4-0.6[g]	100 cycles[d]	21
$[Fe_3O(H_2O)_2F(BTC)_3]$	0.6	44.4	0.2-0.4	yes	40 cycles[d]	20,22,23
$[Al_3O(H_2O)_2F(BTC)_3]$	0.35	43.3	0.2-0.4	yes	40 cycles[d]	20,22
[Al(OH)(FUM)]	0.25	48.4	0.2-0.3	yes	4500 cycles[d]	24
[Al(OH)TDC]	0.35	46.8	0.26	yes	40 cycles[d]	25
[Al(OH)(FDC)]	0.35	54	0.08	no	10 cycles[d]	26
[Al(OH)(*m*-BDC)]	0.30	53.5	0.16	no	10000 cycles[d]	27
[Al(OH)(TDC)]	0.35	48.2	0.26	no	5000 cycles[d]	28
[Al(OH)(PZDC)]	0.35	~49	0.1-0.2	yes	150 cycles	29
$[Zr_6O_4(OH)_4(p\text{-}BDC)_6]^f$	0.4	41.3	0.1-0.4	yes	n.a.	30–33
$[Zr_6O_4(OH)_4(p\text{-}BDC\text{-}NH^2)_6]^f$	0.38	89.5	0.01-0.2	yes	40 cycles[d]	31,33–35
$[Zr_6O_4(OH)_4(BPDC)_6]^f$	0.18	51.7	0.5-0.7	yes	n.a.	33,36
$[Zr_6O_4(OH)_4(FUM)_6]$	0.25	~54	0.05	no	n.a.	29,37–39
$[Zr_6O_4(OH)_2(TDC)_5(AC)_4(H_2O)_4]^f$	0.27	n.a.	0.22-0.4	yes	n.a.	39,40
$[Zr_6O_4(OH)_4(MTB)_2(FA)_4(H_2O)_4]$	0.33	50	0.22	no	n.a.	37,39
$[Zr_6O_4(OH)_4(MDIP)_2(fa)_4]$	0.25	55	0.16	no	3d in $NH_3(g)$	41

[a] usable capacity [b] adsorption step [c] against water [d] under application conditions [e] F, Cl, 0.5 SO_4

[f] may contain linker defects [g] desired for humidity regulation

Tab. S10.1 – continuation

Formula	Capacity[e] [g/g]	$-\Delta H_{ads}$ [kJ/mol]	p_{rel}[b] $[p/p_0]$	Hysteresis	Stability (Water)	Literature
$[Cu_3(BTC)_2(H_2O)_3]$	0.4	50.7	0.05-0.2	yes	Not stable	[34,42,43]
$[Ti_8O_8(OH)_4(p\text{-}BDC\text{-}NH_2)_6]$	0.37	56	0.15	no	40 cycles[h]	[33,44]
$[Co_2Cl_2(BTDD)]$	0.7	45.8	0.3	no	30 h 6 cycles	[45,46]
$[Ni_2Cl_2(BTDD)]$	0.5	n.a.	0.31	no	n.a.	[45,46]
$[Ni_3(BTC)_3(BTRE)_2(H2O)_2]$	0.21	43.9	0.4	n.a.	n.a.	[43,47]
$(DMA)_3[Y_9O_2(OH)_{14}(H_2O)_7(BTEB)_3]$	0.5	n.a.	0.6	0.4 - 0.6[i]	24 h 0.9 p/p_0	[48]
$[Zn(MCIM)_2]$	0.12	n.a.	0.1-0.3	yes	n.a.	[49]
$[Zn(ICA)_2]$	0.29	n.a.	0.3	n.a.	n.a.	[50]
$[SiO_2]$	0.3	55.7	0-0.95	yes	22 cycles	[3,51]
Ti_x-SAPO-34	n.a.	57.6	n.a.	n.a.	n.a.	[52]
$[Si_{0.16}Al_{0.4}P_{0.45}O_2]$[e]	0.3	55.5	0.04	no	6000 cycles[h]	[3,53,54]
$[AlPO_4]$	0.38	55.1	0.1	no	25-cycles	[3,55]
$[AlPO_4]$	0.2	50	0.3	no	n.a.	[56]
$[Fe_xAl_{1-x}PO_4]$[e]	0.2	54	0.2	no	200000[h]	[57]
amorphes Silica	0.7	58	0.4-0.6	yes	n.a.	[53,58]
$Na_x[Al_xSi_{1-x}O_2]$[e]	0.38	61.2	<0.01	no	n.a.	[32,59]
$Na_x[Al_xSi_{1-x}O_2]$[e]	0.25	64.8	<0.01	no	50000[h]	[3,53,60]

[a]usable capacity [b]adsorütion step [c]against water [d]trade name i.e. AQSOA-Z02 [e]ratios may vary

[f]trade name i.e. AQSOA-Z05 [g]trade name i.e. AQSOA-Z01 bzw. FAM-Z01 [h]under application conditions

[i]desired for humidity regulation [j]different pore sizes possible, therefore given as range

Name
MIL-101(Cr)
MIL-100(Cr)
Soc-MOF-1(Cr)
MIL-100(Fe)
MIL-100(Al)
MIL-53-FUM(Al)
MIL-53-TDC(Al)
MIL-160-FDC(Al)
CAU-10-*m*-BDC-H(Al)
CAU-23-TDC(Al)
MIL-53-PZDC(Al)
UiO-66-*p*-BDC(Zr)
UiO-66-*p*-BDC-NH_2(Zr)
UiO-67-BPDC(Zr)
UiO-66-FUM(Zr)
DUT-67(Zr)
MOF-841(Zr)
MIP-200(Zr)

Name
HKUST-1-BTC(Cu)
MIL-125-p-BDC-NH_2(Ti)
Co_2Cl_2BTDD
Ni_2Cl_2BTDD
ISE-1
Y-shp-MOF-5
SIM-1
Z
Silica-Gel
TiAPSO
SAPO-34[d]
AlPO-18
AlPO-5[f]
FAPO-5[g]
MCM-41[j]
Na-Zeolith-13X
Na-Zeolith-Y

References

1 K. Barthelet, D. Riou and G. Férey, *Chem. Commun.*, 2002, 1492–1493.

2 D. J. Xiao, E. D. Bloch, J. A. Mason, W. L. Queen, M. R. Hudson, N. Planas, J. Borycz, A. L. Dzubak, P. Verma, K. Lee, F. Bonino, V. Crocellà, J. Yano, S. Bordiga, D. G. Truhlar, L. Gagliardi, C. M. Brown and J. R. Long, *Nature Chemistry*, 2014, **6**, 590–595.

3 S. K. Henninger, G. Munz, K.-F. Ratzsch and P. Schossig, *Renewable Energy*, 2011, **36**, 3043–3049.

4 Perdew, Burke and Ernzerhof, *Physical review letters*, 1996, **77**, 3865–3868.

5 F. Weigend and R. Ahlrichs, *Phys. Chem. Chem. Phys.*, 2005, **7**, 3297.

6 M. Krack, *Theor Chem Acc*, 2005, **114**, 145–152.

7 S. Grimme, J. Antony, S. Ehrlich and H. Krieg, *The Journal of Chemical Physics*, 2010, **132**, 154104.

8 S. Goedecker, M. Teter and J. Hutter, *Phys. Rev. B*, 1996, **54**, 1703–1710.

9 a) T. A. Manz and D. S. Sholl, *Journal of chemical theory and computation*, 2012, **8**, 2844–2867; b) T. A. Manz and D. S. Sholl, *Journal of chemical theory and computation*, 2010, **6**, 2455–2468;

10 a) P. G. Boyd, Y. Lee and B. Smit, *Nat Rev Mater*, 2017, **2**, 1; b) D. Nazarian, J. S. Camp and D. S. Sholl, *Chem. Mater.*, 2016, **28**, 785–793;

11 S. L. Mayo, B. D. Olafson and W. A. Goddard, *J. Phys. Chem.*, 1990, **94**, 8897–8909.

12 A. K. Rappe, C. J. Casewit, K. S. Colwell, W. A. Goddard and W. M. Skiff, *Journal of the American Chemical Society*, 1992, **114**, 10024–10035.

13 a) W. L. Jorgensen, D. S. Maxwell and J. Tirado-Rives, *Journal of the American Chemical Society*, 1996, **118**, 11225–11236; b) C. D. Wick, J. M. Stubbs, N. Rai and J. I. Siepmann, *J. Phys. Chem. B*, 2005, **109**, 18974–18982;

14 J. L. F. Abascal and C. Vega, *The Journal of Chemical Physics*, 2005, **123**, 234505.

15 T. J. H. Vlugt, E. García-Pérez, D. Dubbeldam, S. Ban and S. Calero, *Journal of chemical theory and computation*, 2008, **4**, 1107–1118.

16 M. P. Allen and D. J. Tildesley, *Computer simulation of liquids*, 1989.

17 a) J. Ehrenmann, S. K. Henninger and C. Janiak, *Eur. J. Inorg. Chem.*, 2011, **2011**, 471–474; b) G. Férey, C. Mellot-Draznieks, C. Serre, F. Millange, J. Dutour, S. Surblé and I. Margiolaki, *Science*, 2005, **309**, 2040–2042;

18 M. F. de Lange, J.-J. Gutierrez-Sevillano, S. Hamad, T. J. H. Vlugt, S. Calero, J. Gascon and F. Kapteijn, *J. Phys. Chem. C*, 2013, **117**, 7613–7622.

19 G. Akiyama, R. Matsuda and S. Kitagawa, *Chemistry Letters*, 2010, **39**, 360–361.

20 Y.-K. Seo, J. W. Yoon, J. S. Lee, Y. K. Hwang, C.-H. Jun, J.-S. Chang, S. Wuttke, P. Bazin, A. Vimont, M. Daturi, S. Bourrelly, P. L. Llewellyn, P. Horcajada, C. Serre and G. Férey, *Advanced Materials*, 2012, **24**, 806–810.

21 S. M. T. Abtab, D. Alezi, P. M. Bhatt, A. Shkurenko, Y. Belmabkhout, H. Aggarwal, Ł. J. Weseliński, N. Alsadun, U. Samin, M. N. Hedhili and M. Eddaoudi, *Chem*, 2018, **4**, 94–105.

22 F. Jeremias, A. Khutia, S. K. Henninger and C. Janiak, *J. Mater. Chem.*, 2012, **22**, 10148–10151.

23 P. Horcajada, S. Surblé, C. Serre, D.-Y. Hong, Y.-K. Seo, J.-S. Chang, J.-M. Grenèche, I. Margiolaki and G. Férey, *Chem. Commun.*, 2007, **27**, 2820–2822.

24 a) E. Alvarez, N. Guillou, C. Martineau, B. Bueken, B. Van de Voorde, C. Le Guillouzer, P. Fabry, F. Nouar, F. Taulelle, D. de Vos, J.-S. Chang, K. H. Cho, N. Ramsahye, T. Devic, M. Daturi, G. Maurin and C. Serre, *Angewandte Chemie*, 2015, **127**, 3735–3739; b) H. W. B. Teo, A. Chakraborty and S. Kayal, *Microporous and Mesoporous Materials*, 2018, **272**, 109–116; c) F. Jeremias, D. Fröhlich, C. Janiak and S. K. Henninger, *RSC Advances*, 2014, **4**, 24073–24082; d) H. Kummer, F. Jeremias, A.

Warlo, G. Füldner, D. Fröhlich, C. Janiak, R. Gläser and S. K. Henninger, *Industrial & Engineering Chemistry Research*, 2017, **56**, 8393–8398;

25 a) N. Tannert, S.-J. Ernst, C. Jansen, H.-J. Bart, S. K. Henninger and C. Janiak, *J. Mater. Chem. A*, 2018, **6**, 17706–17712; b) C. B. L. Tschense, N. Reimer, C.-W. Hsu, H. Reinsch, R. Siegel, W.-J. Chen, C.-H. Lin, A. Cadiau, C. Serre, J. Senker and N. Stock, *Zeitschrift für anorganische und allgemeine Chemie*, 2017, **643**, 1600–1608;

26 a) A. Permyakova, O. Skrylnyk, E. Courbon, M. Affram, S. Wang, U.-H. Lee, A. H. Valekar, F. Nouar, G. Mouchaham, T. Devic, G. de Weireld, J.-S. Chang, N. Steunou, M. Frère and C. Serre, *ChemSusChem*, 2017, **10**, 1419–1426; b) A. Cadiau, J. S. Lee, D. Damasceno Borges, P. Fabry, T. Devic, M. T. Wharmby, C. Martineau, D. Foucher, F. Taulelle, C.-H. Jun, Y. K. Hwang, N. Stock, M. F. de Lange, F. Kapteijn, J. Gascon, G. Maurin, J.-S. Chang and C. Serre, *Advanced Materials*, 2015, **27**, 4775–4780;

27 a) H. Reinsch, M. A. van der Veen, B. Gil, B. Marszalek, T. Verbiest, D. de Vos and N. Stock, *Chem. Mater.*, 2013, **25**, 17–26; b) D. Fröhlich, E. Pantatosaki, P. D. Kolokathis, K. Markey, H. Reinsch, M. Baumgartner, M. A. van der Veen, D. E. de Vos, N. Stock, G. K. Papadopoulos, S. K. Henninger and C. Janiak, *J. Mater. Chem. A*, 2016, **4**, 11859–11869; c) D. Lenzen, P. Bendix, H. Reinsch, D. Fröhlich, H. Kummer, M. Möllers, P. P. C. Hügenell, R. Gläser, S. Henninger and N. Stock, *Advanced Materials*, 2018, **30**, 1705869;

28 D. Lenzen, J. Zhao, S.-J. Ernst, M. Wahiduzzaman, A. Ken Inge, D. Fröhlich, H. Xu, H.-J. Bart, C. Janiak, S. Henninger, G. Maurin, X. Zou and N. Stock, *Nature communications*, 2019, **10**, 3025.

29 F. Fathieh, M. J. Kalmutzki, E. A. Kapustin, P. J. Waller, J. Yang and O. M. Yaghi, *Sci. Adv.*, 2018, **4**, eaat3198.

30 H. Jasuja, J. Zang, D. S. Sholl and K. S. Walton, *J. Phys. Chem. C*, 2012, **116**, 23526–23532.

31 G. E. Cmarik, M. Kim, S. M. Cohen and K. S. Walton, *Langmuir*, 2012, **28**, 15606–15613.

32 M. H. Bagheri and S. N. Schiffres, *Langmuir*, 2018, **34**, 1908–1915.

33 F. Jeremias, V. Lozan, S. K. Henninger and C. Janiak, *Dalton Trans*, 2013, **42**, 15967–15973.

34 P. M. Schoenecker, C. G. Carson, H. Jasuja, C. J. J. Flemming and K. S. Walton, *Ind. Eng. Chem. Res.*, 2012, **51**, 6513–6519.

35 M. Kandiah, M. H. Nilsen, S. Usseglio, S. Jakobsen, U. Olsbye, M. Tilset, C. Larabi, E. A. Quadrelli, F. Bonino and K. P. Lillerud, *Chem. Mater.*, 2010, **22**, 6632–6640.

36 J. H. Cavka, S. Jakobsen, U. Olsbye, N. Guillou, C. Lamberti, S. Bordiga and K. P. Lillerud, *Journal of the American Chemical Society*, 2008, **130**, 13850–13851.

37 M. V. Solovyeva, L. G. Gordeeva, T. A. Krieger and Y. I. Aristov, *Energy Conversion and Management*, 2018, **174**, 356–363.

38 H. Kim, S. Yang, S. R. Rao, S. Narayanan, E. A. Kapustin, H. Furukawa, A. S. Umans, O. M. Yaghi and E. N. Wang, *Science*, 2017, **356**, 430–434.

39 H. Furukawa, F. Gándara, Y.-B. Zhang, J. Jiang, W. L. Queen, M. R. Hudson and O. M. Yaghi, *Journal of the American Chemical Society*, 2014, **136**, 4369–4381.

40 V. Bon, I. Senkovska, I. A. Baburin and S. Kaskel, *Crystal Growth & Design*, 2013, **13**, 1231–1237.

41 S. Wang, J. S. Lee, M. Wahiduzzaman, J. Park, M. Muschi, C. Martineau-Corcos, A. Tissot, K. H. Cho, J. Marrot, W. Shepard, G. Maurin, J.-S. Chang and C. Serre, *Nat Energy*, 2018, **3**, 985–993.

42 a) S. K. Henninger, F. P. Schmidt and H.-M. Henning, *Adsorption*, 2011, **17**, 833–843; b) S. S.-Y. Chui, S. M.-F. Lo, J. P. H. Charmant, A. G. Orpen and I. D. Williams, *Science*, 1999, **283**, 1148–1150;

43 S. K. Henninger, F. Jeremias, H. Kummer and C. Janiak, *Eur. J. Inorg. Chem.*, 2012, **16**, 2625–2634.

44 a) S.-N. Kim, J. Kim, H.-Y. Kim, H.-Y. Cho and W.-S. Ahn, *Catalysis Today*, 2013, **204**, 85–93; b) M. Dan-Hardi, C. Serre, T. Frot, L. Rozes, G. Maurin, C. Sanchez and G. Férey, *Journal of the American Chemical Society*, 2009, **131**, 10857–10859;

45 A. J. Rieth, Y. Tulchinsky and M. Dincă, *Journal of the American Chemical Society*, 2016, **138**, 9401–9404.

46 A. J. Rieth, S. Yang, E. N. Wang and M. Dincă, *ACS Cent. Sci.*, 2017, **3**, 668–672.

47 S. K. Henninger, H. A. Habib and C. Janiak, *Journal of the American Chemical Society*, 2009, **131**, 2776–2777.

48 R. G. AbdulHalim, P. M. Bhatt, Y. Belmabkhout, A. Shkurenko, K. Adil, L. J. Barbour and M. Eddaoudi, *Journal of the American Chemical Society*, 2017, **139**, 10715–10722.

49 a) J. Canivet, J. Bonnefoy, C. Daniel, A. Legrand, B. Coasne and D. Farrusseng, *New J. Chem.*, 2014, **38**, 3102–3111; b) S. Aguado, J. Canivet and D. Farrusseng, *Chem. Commun.*, 2010, **46**, 7999–8001;

50 a) W. Morris, C. J. Doonan, H. Furukawa, R. Banerjee and O. M. Yaghi, *Journal of the American Chemical Society*, 2008, **130**, 12626–12627; b) K. Zhang, R. P. Lively, M. E. Dose, A. J. Brown, C. Zhang, J. Chung, S. Nair, W. J. Koros and R. R. Chance, *Chem. Commun.*, 2013, **49**, 3245–3247;

51 R. L. Yeh, T. K. Ghosh and A. L. Hines, *Journal of Chemical & Engineering Data*, 1992, **37**, 259–261.

52 P. Bendix, G. Füldner, M. Möllers, H. Kummer, L. Schnabel, S. Henninger and H.-M. Henning, *Applied Thermal Engineering*, 2017, **124**, 83–90.

53 J. Jänchen and H. Stach, *Energy Procedia*, 2012, **30**, 289–293.

54 a) B. Dawoud, *Applied Thermal Engineering*, 2013, **50**, 1645–1651; b) A. Frazzica, G. Füldner, A. Sapienza, A. Freni and L. Schnabel, *Applied Thermal Engineering*, 2014, **73**, 1022–1031; c) F. Stallmach, T. Splith, C. Chmelik, G. Füldner, S. K. Henninger, P. T. Kolokathis, E. Pantatosaki and G. K. Papadopoulos, *Chemie Ingenieur Technik*, 2016, **88**, 372–378; d) G. Liu, P. Tian, Y. Zhang, J. Li, L. Xu, S. Meng and Z. Liu, *Microporous and Mesoporous Materials*, 2008, **114**, 416–423; e) A. Freni, L. Bonaccorsi, L. Calabrese, A. Caprì, A. Frazzica and A. Sapienza, *Applied Thermal Engineering*, 2015, **82**, 1–7;

55 a) A. Simmen, L. B. McCusker, C. Baerlocher and W. M. Meier, *Zeolites*, 1991, **11**, 654–661; b) S. K. Henninger, F. P. Schmidt and H.-M. Henning, *Applied Thermal Engineering*, 2010, **30**, 1692–1702;

56 a) B. L. Newalkar, R. V. Jasra, V. Kamath and S.G.T. Bhat, *Microporous and Mesoporous Materials*, 1998, **20**, 129–137; b) Y. G. Bushuev, G. Sastre, J. V. de Julián-Ortiz and J. Gálvez, *J. Phys. Chem. C*, 2012, **116**, 24916–24929; c) P. Bordat, J. Kirstein, P. Labéguerie, M. Merawa and R. Brown, *J. Phys. Chem. C*, 2007, **111**, 10972–10981;

57 a) H. Kakiuchi, S. Shimooka, M. Iwade, K. Oshima, M. Yamazaki, S. Terada, H. Watanabe and T. Takewaki, *KAGAKU KOGAKU RONBUNSHU*, 2005, **31**, 361–364; b) Y.-D. Kim, K. Thu and K. C. Ng, *Desalination*, 2014, **344**, 350–356; c) Pang Wenqin, Qiu Shilun, Kan Qiubin, Wu Zhiyun, Peng Shaoyi, Fan Guochuan and Tian Di, in *Zeolites: Facts, Figures, Future Part A - Proceedings of the 8th International Zeolite Conference*, ed. P.A. Jacobs and R.A. van Santen, Elsevier, 1989, vol. 49, pp. 281–289;

58 P. L. Llewellyn, F. Schueth, Y. Grillet, F. Rouquerol, J. Rouquerol and K. K. Unger, *Langmuir*, 1995, **11**, 574–577.

59 F. B. Cortés, F. Chejne, F. Carrasco-Marín, C. Moreno-Castilla and A. F. Pérez-Cadenas, *Adsorption*, 2010, **16**, 141–146.

60 A. Ristić, F. Fischer, A. Hauer and N. Zabukovec Logar, *J. Mater. Chem. A*, 2018, **6**, 11521–11530.